applied sciences

MDPI

Article

Comparison of Phase-Screen and Geometry-Based Phase Aberration Correction Techniques for Real-Time Transcranial Ultrasound Imaging

Moein Mozaffarzadeh [1,*], Martin D. Verweij [1,2], Nico de Jong [1,2] and Guillaume Renaud [1]

[1] Laboratory of Medical Imaging, Department of Imaging Physics, Delft University of Technology, 2628 CJ Delft, The Netherlands
[2] Department Biomedical Engineering, Thoraxcenter, Erasmus Medical Center, 3015 GD Rotterdam, The Netherlands
* Correspondence: m.mozaffarzadeh@tudelft.nl

Abstract: While transcranial ultrasound imaging is a promising diagnostic modality, it is still hindered due to phase aberration and multiple scattering caused by the skull. In this paper, we compare near-field phase-screen modeling (PS) to a geometry-based phase aberration correction technique (GB) when an ultrafast imaging sequence (five plane waves tilted from −15 to +15 degrees in the cutaneous tissue layer) is used for data acquisition. With simulation data, the aberration profile (AP) of two aberrator models (flat and realistic temporal bone) was estimated in five isoplanatic patches, while the wave-speed of the brain tissue surrounding the point targets was either modeled homogeneously (ideal) or slightly heterogeneously to generate speckle (for mimicking a more realistic brain tissue). For the experiment, a phased array P4-1 transducer was used to image a wire phantom; a 4.2-mm-thick bone-mimicking plate was placed in front of the probe. The AP of the plate was estimated in three isoplanatic patches. The numerical results indicate that, while all the scatterers are detectable in the image reconstructed by the GB method, many scatterers are not detected with the PS method when the dataset used for AP estimation is generated with a realistic bone model and heterogeneous brain tissue. The experimental results show that the GB method increases the signal-to-clutter ratio (SCR) by 7.5 dB and 6.5 dB compared to the PS and conventional reconstruction methods, respectively. The GB method reduces the axial/lateral localization error by 1.97/0.66 mm and 2.08/0.7 mm compared to the PS method and conventional reconstruction, respectively. The lateral spatial resolution (full-width-half-maximum) is also improved by 0.1 mm and 1.06 mm compared to the PS method and conventional reconstruction, respectively. Our comparison study suggests that GB aberration correction outperforms the PS method when an ultrafast multi-angle plane wave sequence is used for transcranial imaging with a single transducer.

Keywords: transcranial ultrasound imaging; phase aberration correction; near-field phase-screen modeling; adaptive beamforming; temporal bone

check for updates

Citation: Mozaffarzadeh, M.; Verweij, M.D.; de Jong, N.; Renaud, G. Comparison of Phase-Screen and Geometry-Based Phase Aberration Correction Techniques for Real-Time Transcranial Ultrasound Imaging. *Appl. Sci.* **2022**, *12*, 10183. https://doi.org/10.3390/app121910183

Academic Editors: Jürgen W. Czarske, Richard Nauber and Lars Buettner

Received: 7 July 2022
Accepted: 7 October 2022
Published: 10 October 2022

1. Introduction

Transcranial ultrasound imaging (TUI) is used in hospitals for stroke diagnosis [1–7], prevention of stroke in children (between an age of 2 and 16) with sickle cell disease [8–10], and detection of vasospasm after subarachnoid hemorrhage (most often caused by head trauma) [11,12]. Yet, the strong wave aberration [13] and multiple scattering caused by the skull [14,15] are ignored in the current commercial TUI devices, which degrade image quality. This paper focuses on correction of phase aberration caused by the skull.

The temporal window of the skull is usually used for TUI due to its relatively lower attenuation because it consists most often of a single layer of cortical bone with a thickness ranging from 1.5 mm to 4 mm [16]. Two categories of technique were proposed to correct phase aberration: (1) near-field phase-screen modeling [17–19], and (2) the approach relying on estimation of wave-speed, position, and geometry of the bone layer. In near-field phase-screen (PS) approaches, the temporal bone is modeled as an infinitesimally thin aberrating layer at the surface of the transducer [17–19]. The limitation of this method is that correction is only limited to certain regions called isoplanatic patches [14,20–23], in particular because the effect of refraction is ignored. In the second category, the true position, geometry, and sound speed of the temporal bone are estimated prior to image reconstruction either by ultrasound measurements [24–26] or CT/MRI scans of the skull, and then phase aberration, including the effect of refraction, is corrected during image reconstruction [27–30]. Recently, we demonstrated the feasibility of a geometry-based (GB) aberration correction technique for single-sided two-dimensional transcranial ultrasound through the human temporal window using a single handheld commercial probe [31]. Our approach does not require any CT/MRI scan of the skull; the position and geometry of the bone layer are estimated in the ultrasound image. This approach was also used before for in vivo imaging of the inner structure of the radius and tibia bones [32,33]. In Ref. [31], a fast marching technique to solve the Eikonal equation was used for ray-tracing and accurate estimation of the travel-times between image pixels and elements of the array. However, this computationally expensive implementation prevented application of our approach for real-time imaging. To address this issue, a resource-efficient and accelerated ray-tracing approach was proposed in Ref. [34]. With implementation on a graphics processing unit (GPU), real-time GB aberration correction TUI became feasible and was named accelerated refraction-corrected (ARC) image reconstruction. Others [24,25,27,30] used the same geometry-based strategy but utilized a CT scan to obtain the geometry and sound speed of the skull. Real-time imaging was also not doable. In Ref. [26], a focused wave was used in transmission, which is out of the scope of this manuscript. In Refs. [28,29], a focused wave was used in transmission and a CT scan was used to obtain the geometry and sound speed of the skull. Our method estimates the position, geometry, and sound speed of the bone layer with ultrasound (no need for a CT or MRI scan) and using one probe [31] and enables real-time imaging [34].

Our method estimates the position, geometry, and sound speed of the bone layer with ultrasound (no need for a CT or MRI scan) and using one probe [31] and enables real-time imaging [34].

In this work, we aim to compare the PS approach and the ARC-GB aberration correction technique when an ultrafast imaging sequence (transmission of five multi-angle plane waves) is used for data acquisition and real-time imaging with a single probe. This paper shows that the ARC-GB method results in higher image quality compared to the PS method. Unlike the PS method, the ARC-GB method is not affected by the speckle caused by brain tissue heterogeneity.

2. Materials and Methods

A block diagram is provided in Figure 1 to show the steps needed for correcting the phase aberration caused by a bone layer in front of the ultrasound probe using the ARC-GB and PS methods. Synthetic transmit focusing is necessary for the PS method as an ultrafast imaging sequence is used for data acquisition and not a set of transmit-focused waves (traditional line-by-line ultrasound imaging). The images titled "conventional" throughout the paper are reconstructed with conventional delay-and-sum image reconstruction technique, i.e., assuming a medium with uniform wave-speed equal to 1600 m/s, therefore ignoring phase aberration caused by the bone layer.

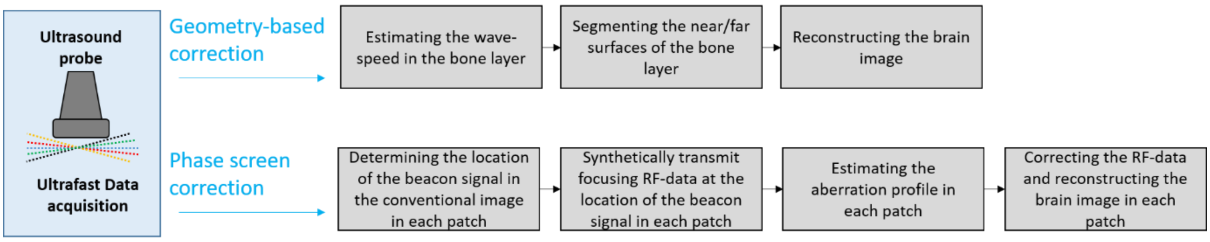

Figure 1. The block diagram showing the processing procedure for the geometry-based and phase-screen aberration correction techniques when an ultrafast imaging sequence (multi-angle plane wave) is used for data acquisition.

2.1. Accelerated Refraction-Corrected Geometry-Based Phase Aberration Correction

We extensively described and evaluated the ARC-GB approach in Ref. [34]. In summary, it consists of 4 steps:

(1) Estimation of the wave-speed in the bone layer with the bidirectional head-wave technique or the autofocus technique [32].
(2) Intermediate points (IPs) are defined on the outer surface of the silicone rubber (called SIPs), the shortest travel-time from pixels in the superficial soft tissue layer to the array elements through the SIPs is found, the image of the superficial soft tissue layer is reconstructed using the calculated travel-times, and the near-surface of the bone layer is segmented using Dijkstra's algorithm [35].
(3) IPs are defined on the near-surface of the bone layer (called NIPs), the shortest travel-time from pixels in the bone layer to array elements through the NIPs is found, the image of the bone layer is reconstructed using the calculated travel-times, and the far-surface of the bone layer is segmented using Dijkstra's algorithm.
(4) IPs are defined on the far surface of the bone layer (called FIPs), the shortest travel-time from pixels in the brain to array elements through the FIPs is found, and the brain image is reconstructed using the calculated travel-times.

For reconstruction, a modified delay-and-sum algorithm (as explained in Refs. [31–33]) was used. The thickness and the wave-speed in the silicone rubber layer can be found either by ultrasound measurements or the datasheet provided by the probe manufacturer. The image reconstruction depth used in steps 2 and 3 can be determined based on prior knowledge of the thickness of the skin and bone layers [36]. The terms "near surface" and "far surface" are defined with respect to the probe. The results captioned "Geometry-based paper" are generated with the ARC-GB reconstruction technique.

2.2. Near-Field Phase-Screen Approach

The PS correction technique requires a coherent wavefront backscattered from a small volume for estimating the aberration profile (AP) in each isoplanatic patch. Such a coherent wavefront backscattered from a small volume can be obtained if ideal echogenic point reflectors exist (such as microbubbles [37]) throughout the and/or thanks to transmit focusing in the heterogeneous medium [38,39]. Transmit focusing is obtained by true transmission of focused waves or by synthetic transmit focusing (post-processing) if a set of unfocused waves (plane or diverging waves) are transmitted. In this paper, we evaluate the microbubble scenario (a more ideal situation for the PS method). Following steps are taken to determine the AP of an isoplanatic patch:

(1) An image is reconstructed using a conventional delay-and-sum reconstruction technique (see Figure 2a), i.e., assuming a medium with uniform wave-speed equal to 1600 m/s. Then, we estimate the coordinates of the echogenic scatterers (used to estimate the AP of the isoplanatic patch), indicated by the green dots in Figure 2a. Note that these coordinates are not the true coordinates of the targets (the red dots in Figure 2a) because phase aberration is ignored in conventional image reconstruction.

(2) For synthetic transmit focusing, transmit time delays for the transmit unfocused waves to reach simultaneously the coordinates of the echogenic scatterer found in step 1 are calculated. Then, the RF data acquired separately with each transmit unfocused wave are shifted by the calculated transmit delay.

(3) By summing all the shifted RF data, RF data with transmit focusing are synthetically generated. As a result, the wavefront backscattered from the chosen scatterer has a higher amplitude compared to wavefronts backscattered by other scatterers and the unfocused RF data (compare the amplitude of the backscattered wavefront from scatterer #1 and #2 in Figure 2b,c, where the amplitude of scatterer #2 in panel (c) is three times higher than from panel (b)).

(4) The receive travel-times between the location of the scatterer and the array elements are calculated by triangulation (the green-dashed line in Figure 2c) assuming a medium with uniform wave-speed equal to 1600 m/s. They are used to define a time mask with which the backscattered wavefront in the RF data after synthetic transmit focusing is extracted (Figure 2d).

(5) A-lines of the extracted wavefront in step 4 are summed up over all elements of the array to obtain a reference signal (see Ref. SIG in Figure 2e), also known as beamsum reference signal [40]. Then, the phase shift between each A-line and the reference signal is calculated and unwrapped to compensate for phase jumps (Figure 2f). This results in the AP in the isoplanatic patch.

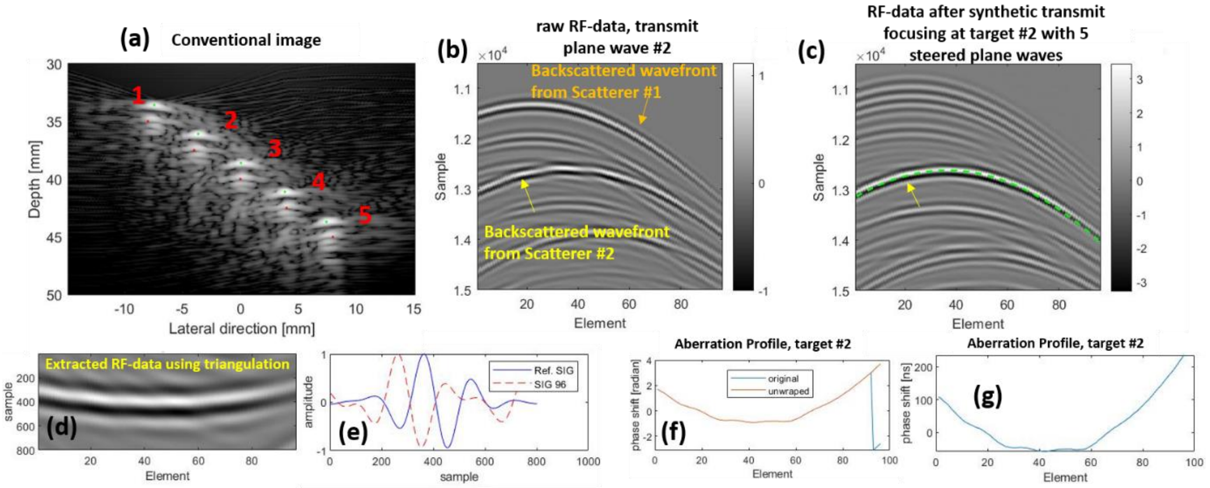

Figure 2. (**a**) The reconstructed image using the conventional delay-and-sum beamformer; the aberrator model and phantom shown in Figure 3a,c were used to generate the numerical RF data. (**b**) The numerical wavefront backscattered from scatterer #2 for a tilted (by 7.5 degrees in cutaneous tissue) transmit plane wave. (**c**) The numerical wavefront after synthetic transmit focusing at the location of scatterer #2 by coherent compounding of the RF data obtained with 5 tilted plane waves (from −15 to 15 degree in cutaneous tissue). (**d**) The extracted wavefront using triangulation assuming a uniform medium. (**e**) The reference signal and the A-line received by element 96 of the array. (**f**) The estimated phase shifted and its unwrapped version for each element. (**g**) The estimated phase shift (aberration profile) in nanoseconds for the isoplanatic patch around target #2. The red and green dots in (**a**) indicate the true location of the scatterers and the brightest pixel in the conventional image that is actually used to apply the PS method, respectively. The red numbers in (**a**) are used for referencing in the text.

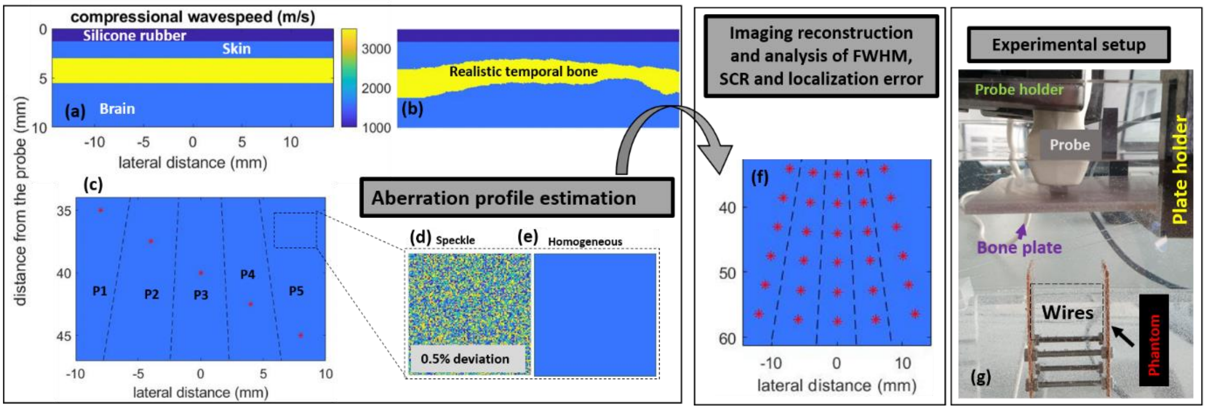

Figure 3. (**a**,**b**) The layered medium used in the simulation with a flat bone layer or a realistic temporal bone. (**c**) The numerical phantom used for estimating the aberration profile in each isoplanatic patch (P1–P5); the dashed lines separate isoplanatic patches. (**d**) The heterogeneous and (**e**) homogeneous background wave-speed model used in the simulations conducted for aberration profile estimation. (**f**) The numerical phantom used to generate the dataset needed for analysis of the full-width at half-maximum (FWHM), the signal-to-clutter ratio (SCR), and localization error. (**g**) The experimental setup to image a wire phantom while a bone mimicking plate is positioned in front of a phased array.

It should be noticed that a uniform-tissue medium is assumed in all the above steps. The AP of each isoplanatic patch is calculated separately based on the wavefront backscattered from the scatterer positioned in the isoplanatic patch. It is used to correct the arrival time of the raw RF data before applying a conventional beamformer to reconstruct the image. The results captioned "phase-screen" throughout the paper are those generated with the near-field phase-screen modeling technique.

2.3. Numerical Study

The k-Wave MATLAB toolbox was used to evaluate the PS and GB reconstruction techniques in a two-dimensional (2D) lossless medium, ignoring generation of shear waves [41]. Our numerical study on the PS method consists of two steps: (1) estimating the AP of each isoplanatic patch using an ideal phantom for PS technique (see the left box in Figure 3) and (2) applying the estimated AP on the RF data generated using a phantom with 30 small scatterers at different lateral and axial locations (see Figure 3f) and analyzing the image.

For step 1, two aberrator models and two background wave-speed models provide four scenarios (four datasets): (1) a flat bone (Figure 3a) and a homogeneous background (Figure 3e), (2) the flat bone and a heterogeneous background generating speckle (Figure 3d), (3) a realistic bone (based on the micro CT of a human temporal bone (provided by Jing and Lindsey [42])) and homogeneous background, and (4) the realistic bone and a heterogeneous-background-generating speckle. The homogeneous background is an ideal situation for the PS method since individual responses of echogenic targets can be clearly identified in the RF data. This resembles a scenario where the echoes from individual contrast agent microbubbles are used as beacon signal. The wave-speed in Figure 3f randomly varies by +/−0.5% with a uniform distribution with respect to the homogeneous model and mimics realistic brain tissue [43]. Five isoplanatic patches were defined (Figure 3c) by positioning the scatterers at lateral/axial coordinates of −8/35 mm, −4/37.5 mm, 0/40 mm, 4/42.5 mm, 8/45.5 mm, one in each isoplanatic patch. The numerical phantom used for estimating the AP (Figure 3c) was designed such that the hyperbolic wavefront of a scatterer in an isoplanatic patch (acting as a beacon signal) does not interfere with that of another scatterer in another isoplanatic patch; different axial and lateral locations of the scatterers ensured that. This is a very ideal situation for the PS method and most likely not the case in practice where the backscattered wavefront from contrast agent microbubbles is used for AP estimation, even if a small volume of contrast agent is injected.

For step 2 (image analysis), the two aberrator models, a homogeneous background and the phantom shown in Figure 3f, where 30 scatterers were positioned in different axial and lateral locations within each patch, were used to generate a numerical dataset. These two additional datasets were used for quantitative evaluation of both the PS and GB methods.

The speed of sound (compressional wave-speed) in the silicone rubber, skull, and soft tissue (cutaneous tissue and brain tissue if homogeneous) was 1000 m/s, 3200 m/s, and 1600 m/s, respectively. The mass density of the soft tissue/silicone rubber and skull was 1000 kg/m^3 and 1900 kg/m^3, respectively. The thickness of the silicone rubber, cutaneous tissue, and flat bone layers was 1.3 mm, 1.7 mm, and 2.5 mm, respectively. The minimum and maximum thickness of the realistic bone layer was 2.38 mm and 1.2 mm, respectively. The properties of a P4-1 phased-array transducer (ATL/Philips, 2.5 MHz, 96 elements, pitch = 0.295 mm) and 5 plane waves from −15 to +15 degrees (in cutaneous tissue) were used to generate the numerical datasets. The spatial grid and time step sizes were 10 µm and 2 ns, respectively, to minimize numerical dispersion and maintain the stability and accuracy of the simulation.

2.4. Experimental Study

Our experimental setup includes a 4.2-mm-thick bone-mimicking plate (Sawbones, Pacific Research Laboratory, Inc., Vashon, WA, USA) immersed in water (see Figure 3g). A phased-array transducer (P4-1, ATL/Philips, 2.5 MHz, 96 elements, pitch = 0.295 mm) connected to a Vantage 256 system (Verasonics Inc., Kirkland, WA, USA) was used to image a phantom including 6 wires with a diameter of 50 µm, with the bone-mimicking plate positioned at a depth of 5.7 mm in front of the probe and angled at 3.3 degrees; this plate has transverse isotropic elasticity; however, the image plane was chosen perpendicular to the symmetry axis of the material (orientation of the glass fibers); the compressional wave-speed in this plane is isotropic. As the imaging plane of the 1D probe was perpendicular to the phantom wires, the wires are expected to act as point scatterers considering their small diameter (about one-tenth of the wavelength at the central frequency). Five transmit plane waves with steering angles from −15 to +15 degrees (in water) were used for data acquisition. Three isoplanatic patches were used for AP estimation and reconstruction. In our experimental study, the same dataset was used for estimation of the AP with the PS method estimation and image analysis.

2.5. Evaluation Metrics

Lateral spatial resolution calculated as the full-width-half-maximum (FWHM), signal-to-clutter ratio (SCR), and localization errors were used for quantitative evaluation. The SCR was the ratio of the maximum scatterer intensity and the mean clutter intensity in the image background; it is reported in decibels (dBs). In experimental and numerical studies, the localization errors were calculated with respect to the ground truth image, which was generated without an aberrator in front of the probe (not shown here) and the true coordinates of the scatterer. For the numerical study, the evaluation metrics reported for the PS method were calculated when the AP of each patch was estimated with the dataset generated with a homogeneous background, i.e., the most favorable scenario for the PS method. The FWHMs and SCRs reported in the text are mean values obtained for all the scatterers unless stated otherwise.

3. Results

3.1. Numerical Simulations

Our numerical study shows that the AP estimated in each patch (see the scatterers and patches in Figure 3c) varies significantly (see Figure 4a,b). For the flat bone model, the AP significantly varies even if the aberrator is laterally invariant (the plate has a constant thickness and is parallel to the probe array) because the depth and lateral coordinate of the targets are not constant. A shallower target depth (patch #1) leads to a stronger aberration magnitude. An asymmetrical AP is obtained if the target is far from the bisector of the array. The irregular APs in Figure 4b and larger phase shift compared to Figure 4a come from the irregularities of the realistic bone model in its near and far surfaces and its asymmetric shape. Note that the aberration profiles in patches 1 and 2 are not accurately estimated for elements 75 to 96 (see Figure 4b,d) because the phase jump between the beamsum reference signal and the recorded wavefronts are larger than 2π and thus not properly captured with the beamsum channel correlation method [40].

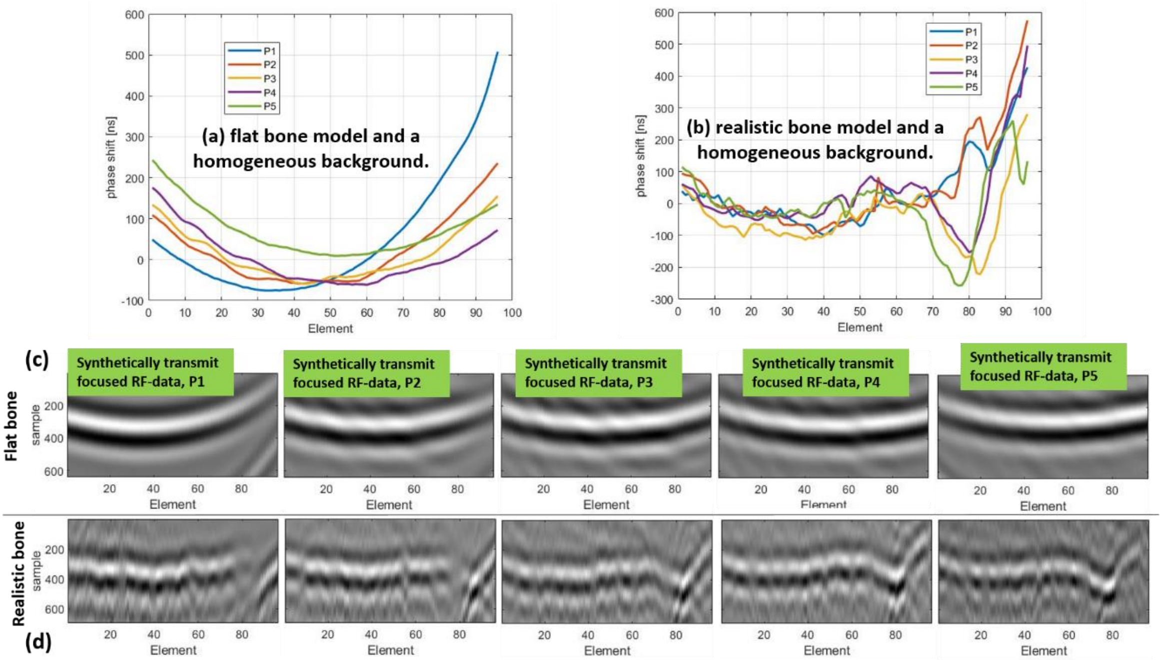

Figure 4. The aberration profile in five isoplanatic patches (indicated by P) when the aberrator/background model is (**a**) flat/homogeneous and (**b**) realistic/heterogeneous. The extracted synthetic-transmit-focused RF data in different isoplanatic patches for the (**c**) flat bone and (**d**) realistic bone model; the background was homogeneous.

Both the PS and GB techniques improve the FWHM compared to the conventional method (compare Figure 5b,d with Figure 5a). For the flat bone and realistic bone models, Table 1 indicates that the PS technique improves the FWHM by 0.18 mm and 0.14 mm compared to the conventional reconstruction, respectively. The GB reconstruction further improves the FWHM compared to the conventional PS method by about 0.08 mm and 0.25 mm, respectively. The most significant improvement obtained by the GB method is the reduced background clutter (compare Figure 5d,b; see Figure 5f for more detail). Table 1 indicates that the GB method improves SCR by 4.9 dB and 2.4 dB compared to the PS technique for the flat and realistic bone model, respectively. The PS method improves the SCR by 4 dB and 4.3 dB compared to the conventional method for the flat and realistic bone model, respectively.

The GB reconstruction technique detects the scatterers at their correct location (compare the location of the scatterers with the red dots in Figure 5d,g for more details). As Table 1 indicates, the GB technique reduces the localization axial error by 1.2–1.3 mm and the localization lateral error by about 0.3 mm compared to conventional reconstruction. In contrast, the PS method does not significantly reduce the localization axial/lateral error compared to the conventional method.

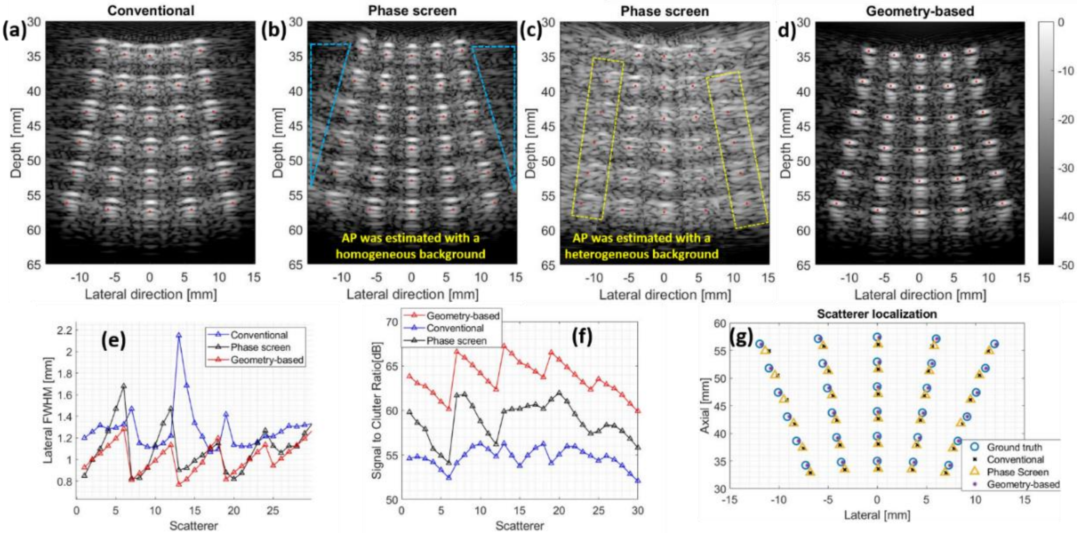

Figure 5. The reconstructed numerical images using (**a**) conventional beamforming, (**b**,**c**) phase-screen modeling, and (**d**) geometry-based reconstruction techniques with a flat bone model (Figure 3a). The aberration profile (AP) was estimated using the dataset generated with a (**b**) homogeneous and (**c**) heterogeneous background wave-speed model. The red dots indicate the true location of the scatterers. The blue triangles in (**b**) indicate the region that was used as background for quantifying the signal-to-clutter ratio calculation in Table 1. The yellow boxes in (**c**) indicate the regions at which the scatterers are completely missed. The lateral FWHM (**e**) and signal-to-clutter ratio (**f**) and localization error (**g**) obtained with all the methods for each scatterer.

Table 1. Quantitative evaluation of the numerical and experimental results presented in Figures 4, 6 and 7.

Method	Metric	[Axial, Lateral] Localization Error (mm)	FWHM (mm)	Signal-to-Clutter Ratio (dB)
Simulation (flat bone)	Conventional	[1.34, 0.42]	1.27 ± 0.20	54.7 ± 1.1
	Phase-screen	[1.31, 0.37]	1.09 ± 0.21	58.7 ± 2.1
	Geometry-based	[0.03, 0.14]	1.01 ± 0.14	63.6 ± 1.9
Simulation (realistic bone)	Conventional	[1.26, 0.90]	1.55 ± 0.52	44.9 ± 2.2
	Phase-screen	[1.05, 0.85]	1.41 ± 0.28	49.2 ± 3.0
	Geometry-based	[0.08, 0.64]	1.16 ± 0.47	51.6 ± 3.1
Sawbones plate	Conventional	[2.23, 0.80]	2.26 ± 0.80	45.1 ± 5.3
	Phase-screen	[2.12, 0.76]	1.30 ± 0.17	44.1 ± 6.0
	Geometry-based	[0.15, 0.10]	1.20 ± 0.28	51.6 ± 5.62

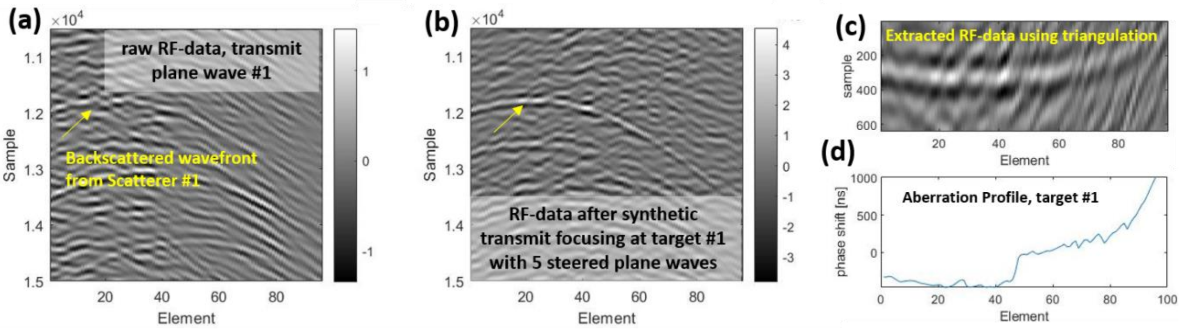

Figure 6. *Cont*.

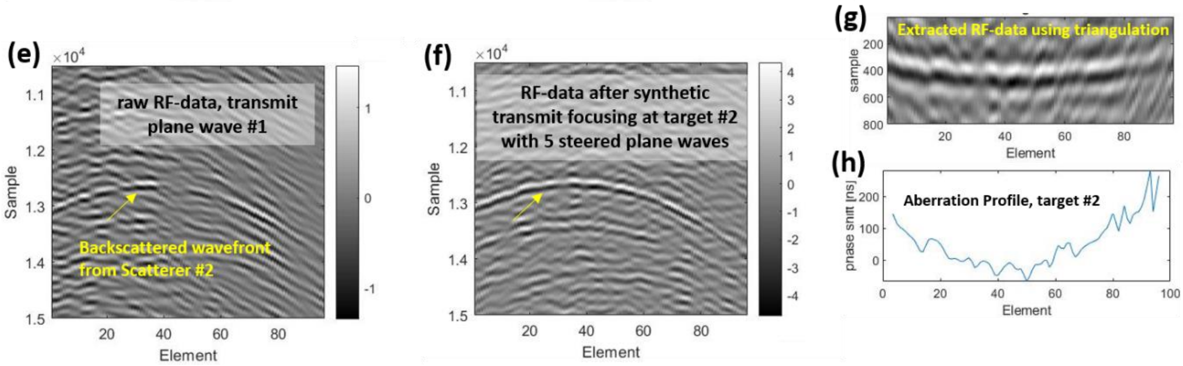

Figure 6. Estimation of the aberration profile with the numerical dataset generated with the flat bone model and a heterogeneous background. The wavefront backscattered from (**a**) scatterer #1 and (**e**) scatterer #2; a tilted plane wave (by 7.5 degrees in cutaneous tissue) was used for excitation. The numerical wavefront backscattered by (**b**) scatterer #1 and (**f**) scatterer #2 after synthetic transmit focusing on the locations of scatterer #1 and #2, respectively, by coherent compounding of the RF data generated by 5 tilted plane waves (from −15 to 15 degree in cutaneous tissue). (**c**,**g**) The extracted wavefront using triangulation for scatterer (**c**) #1 and (**g**) #2. The estimated phase shift (aberration profile) in nanoseconds for scatterer (**d**) #1 and (**h**) #2.

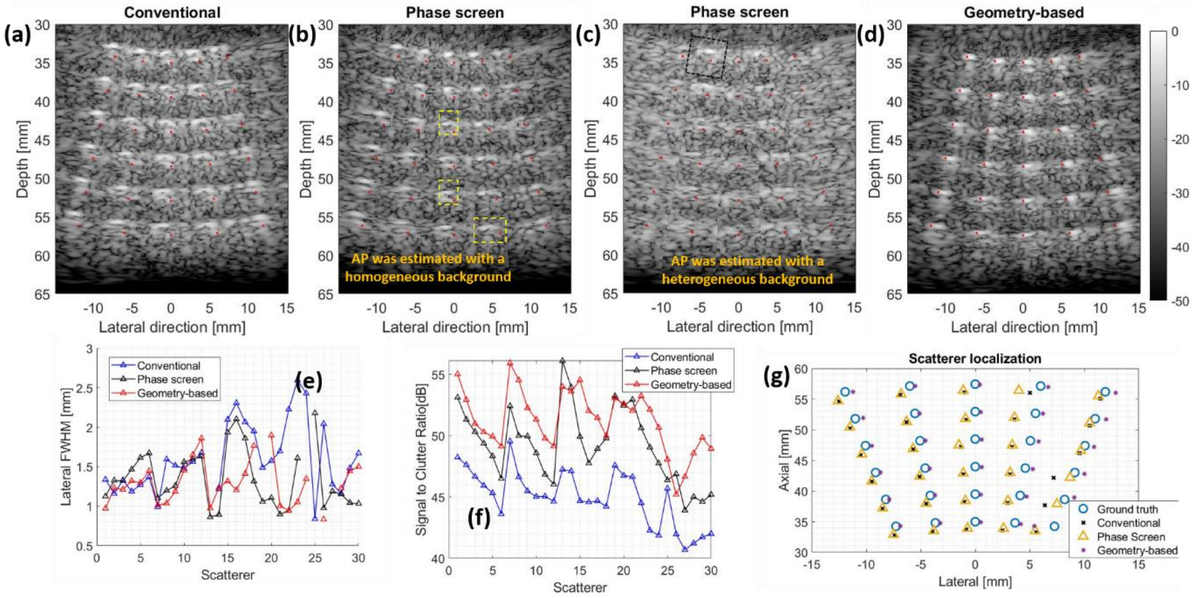

Figure 7. The reconstructed numerical images using (**a**) conventional beamforming, (**b**,**c**) phase-screen modeling, and (**d**) geometry-based reconstruction techniques with a realistic bone model (Figure 3b, based on the micro CT of a real human temporal bone). The aberration profile was estimated using a dataset generated with a (**b**) homogeneous and (**c**) heterogeneous background wave-speed model. The red dots indicate the true location of the scatterers. The lateral FWHM (**e**), the signal-to-clutter ratio (**f**), and the localization error (**g**) obtained with all the methods for each scatterer.

Figure 5c shows the reconstructed image by the PS method when the AP used for phase aberration correction by the PS method is estimated with a heterogeneous background wave-speed model. Many scatterers (see the yellow boxes) are undetectable due to the low accuracy of the aberration profile estimation. As shown in Figure 6f, the focused RF data of the second scatterer (acting as the beacon signal for patch two; see Figure 3c) are better distinguished from the background speckle noise (caused by variation in the background wave-speed speed) compared to the focused RF data of the first scatterer (see Figure 6b). This helps with better estimating the aberration profile and results in better reconstruction of the scatterers in patch 2 compared to patch 1 (Figure 5c). Speckle noise affects each A-line and the reference beamsum signal (which is generated by summation over the A-lines recorded by all the elements of the array), and, consequently, the AP estimation; compare the AP in Figures 2d and 6g and the fine AP in Figures 2g and 6h.

The irregular near and far surfaces of the realistic human temporal bone model (see Figure 3b) degrade the image reconstructed by all the methods. Meanwhile, nearly all the scatterers are detected in the image reconstructed by the GB method (see Figure 7d); most scatterers are not detected by the PS method when the AP is estimated with a homogeneous background (see Figure 7b).

Despite the irregular near and far surfaces of the realistic bone model, Figure 7e and Table 1 indicate that the GB method improves the FWHM, SCR, and localization error compared to the conventional and PS methods.

3.2. Experiments

As the background is water in our experiment, the wavefronts backscattered by the wires are well-detected, and the signal quality is, therefore, excellent to estimate the AP with the PS method. The GB method results in higher image quality (see Figure 8d), although the geometry and position of the bone-mimicking plate are accurately described during image reconstruction with ARC reconstruction. Different results are obtained by switching from AP estimated with scatterers 4 and 6 in Figure 8b to scatterers 3 and 5 in Figure 8c. The image of scatterers 2 and 3 is improved in Figure 8c compared to Figure 8b since the AP for the central patch was estimated with scatterer 3, and scatterer 2 is closer to scatterer 3 than 4. This suggests that the actual size of the central isoplanatic patch is close to 10 mm; therefore, more than three isoplanatic patches may be required to obtain optimal image quality with the PS method. Table 1 indicates that the PS method improves the FWHM by 0.96 mm compared to the conventional reconstruction. FWHM was slightly improved (0.1 mm) with the GB method compared to the PS method.

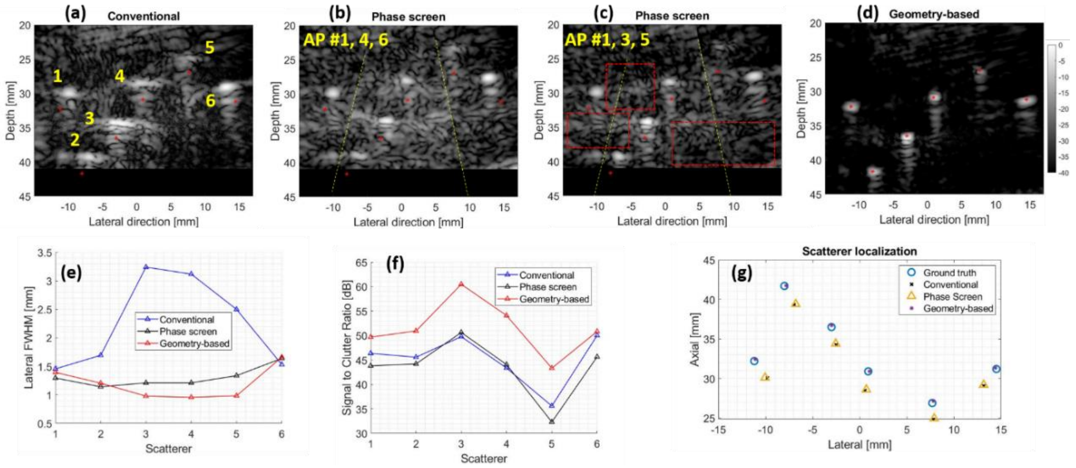

Figure 8. The reconstructed experimental images using the (**a**) conventional beamforming, (**b**,**c**) phase-screen modeling, and (**d**) geometry-based reconstruction techniques when a Sawbones plate was used in front of the probe as an aberrator. The aberration profiles (AP) of scatterer 4/6 and 3/5 were used in (**b**,**c**), respectively. The lateral FWHM (**e**), the signal-to-clutter ratio (**f**), and the localization error (**g**) obtained with all the methods for each scatterer. The red dashed boxes were used for signal-to-clutter ratio calculation in Table 1. The red dots indicate the true location of the scatterers. The numbers in (**a**) are used for referencing in the text and (**e**–**g**).

The GB method increases the SCR by 6.5 dB and 8.2 dB compared to the conventional and PS methods (see Table 1 and Figure 8f), respectively, and reduces the axial/lateralization error by 2.21/0.7 mm (see Table 1) compared to the conventional method. The SCR obtained by the PS method is 1 dB lower than the conventional reconstruction.

4. Discussion

4.1. Advantages and Limitations of the Near-Field Phase-Screen Technique for Ultrafast Transcranial Ultrasound

4.1.1. Advantages

In the PS method, there is no need for describing the medium and imaging the aberrator in order to estimate its position and geometry, and, therefore, it may perform better than GB for a thin temporal bone ($\leq$1 mm thick) at 2.5 MHz. As indicated by Table 1, the PS method improves the lateral spatial resolution and contrast (signal-to-clutter ratio) compared with the conventional image reconstruction technique. The lower SCR obtained by the PS method in the experimental results could mainly be due to the relatively lower clutter obtained with conventional reconstruction in the region indicated by the right red box in Figure 8c.

4.1.2. Limitations

With only five unfocused transmit beams (ultrafast ultrasound imaging), injection of contrast agent microbubbles is required to generate beacon signals because synthetic transmit focusing of speckle with only five plane waves does not generate a strong enough coherent wavefront.

A real-time implementation was achieved with focused transmit beams (three frames/s abdominal scanning [40]) without injection of a contrast agent. However, real-time implementation with injection of a contrast agent and using bubble echoes as beacon signals (post-processing in Ref. [37]) was never reported, and is likely very challenging because automatic detection of bubble position would be necessary. The stronger the aberration, the smaller the size of the isoplanatic patch, and the more isoplanatic patches are required to improve image quality, which means that many APs must be estimated (one per isoplanatic patch; see the change in the quality of the image of scatterers #2 and #5 in Figure 8b,c). This imposes a tradeoff between the image quality and computational time.

The PS method does not improve localization error, especially in depth (panel g in Figures 5, 6 and 8). This is because the PS method uses the information of an already miss-located scatterer (acting as the beacon signal), and, therefore, it does not compensate for the overall error in the calculated travel-time caused by the higher wave-speed in bone. As shown in Figure 9, the PS leads to a travel-time similar to that calculated in the conventional reconstruction. This ambiguity in the overall travel-time (depth ambiguity) leads to suboptimal image reconstruction.

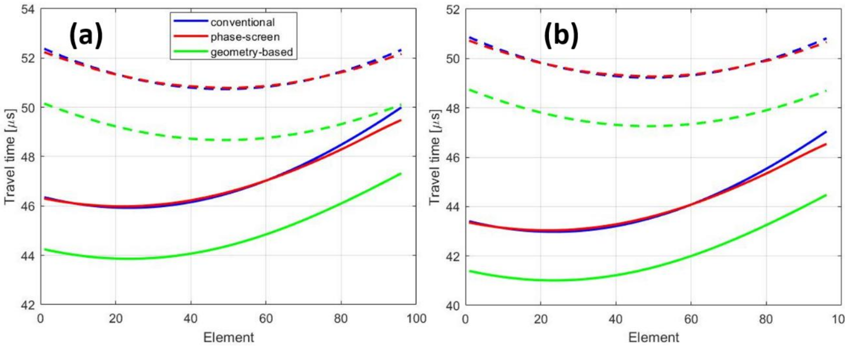

Figure 9. The travel-time estimated for scatterer 1 (solid lines) and scatterer 3 (dashed lines) positioned in patch 1 and 3, respectively (see Figure 3c), with the three different reconstruction techniques when a steered plane wave at (**a**) −15 degree and (**b**) 0 degree is used for transmission. The bone and background models were flat and homogeneous, respectively.

As indicated by the numerical results in Figure 6, accurate estimation of the AP with the beamsum channel correlation method when the brain tissue has a heterogeneous wave-speed is very challenging if the amplitude of the beacon signal is not high enough. The image quality obtained by the PS method in this scenario is poor (panel c in Figures 5 and 6).

4.2. Advantages and Limitations of the Geometry-Based Phase Aberration Correction Technique for Ultrafast Transcranial Ultrasound

4.2.1. Advantages

The GB method improves the lateral spatial resolution, signal-to-clutter ratio, and localization error compared to the PS and conventional reconstruction techniques (see Table 1). It provides an optimal phase aberration correction everywhere in image as the true location and geometry of the aberrator is used to correct the phase aberration (see panel d in Figures 5, 7 and 8). In a previous publication [34], our group demonstrated that the GB method has the potential to enable real-time transcranial imaging (>10 frames/s) without injection of a contrast agent, and its performance is not affected by the heterogeneity (speckle) of the brain tissue; it only requires estimating the position and geometry of the bone layer, as shown in our previous publications [31–33,44]. The GB method is not limited to a maximum bone thickness as long as the attenuation caused by a thick bone layer allows detection of echo signals with sufficient signal-to-noise ratio.

4.2.2. Limitations

The GB method needs to reconstruct an image of the aberrator in order to estimate its position and geometry. This is a challenging task for a thin temporal bone (1 mm thick) at 2.5 MHz because the near and far interfaces of the bone layer cannot be clearly distinguished. Accurate estimation of travel-times also requires an estimate (with the head-wave or the autofocus techniques [32]) or a guess (based on literature) of the wave-speed in each layer while each layer is assumed homogeneous. The assumption of homogeneous tissue layers likely breaks down in individuals with a heterogeneous complex cutaneous tissue layer or a temporal bone containing a diploe.

4.3. Limitations in the Implementation of the Near-Field Phase-Screen Technique in This Work, Possible Improvements

The near-field phase-screen aberration correction technique was most often applied with focused transmit waves [40]. However, to capture the transient fast phenomena in the brain (the blood velocity in the main cerebral arteries can approach 2 m/s [37]) and enable real-time feedback during clinical scans, an ultrafast imaging sequence relying on transmission of unfocused beams is preferred. Thus, the backscattered waves should be synthetically focused in transmit (for generating the coherent wavefront backscattered from a small volume) [37] so that the wavefront from a scatterer in an isoplanatic patch becomes well-distinguished from the background speckle noise and aberration profile estimation with the PS method is feasible. The focusing procedure includes delaying the RF data acquired by transmitting with each unfocused beam with respect to the focal point and coherent summation.

Five steered plane waves are not optimal for efficient synthetic transmit focusing and, therefore, for estimating the aberration profile in each patch accurately. A better approach for the PS method would be to first estimate the APs in each patch with a large number (e.g., 50) of steered plane waves (or diverging waves) combined with synthetic transmit focusing or using focused transmit waves, and then using the estimated APs to correct the phase aberration in each patch when imaging with a high frame rate imaging sequence. Additionally, the PS approach can perform better if applied iteratively by improving transmit focusing at each step [40]. In this work, we used five transmit plane waves and a single estimation of the aberration profile to enable real-time imaging and live feedback to the operator. Moreover, we implemented the PS method with the beamsum channel correlation method; other techniques to estimate the AP, such as the multilagleast-squares cross-correlation method ([21]), may perform better.

The main limitation of this study is that the aberrator was invariant in the out-of-plane dimension, while the temporal bone has a complex three-dimensional shape. Our study considered two-dimensional imaging with a phased-array transducer. However, as demonstrated earlier [21–23,40], a two-dimensional matrix array transducer is required for efficient phase aberration correction with the PS method.

4.4. Limitations in the Implementation of the Geometry-Based Aberration Correction Technique in This Work, Possible Improvements

In this paper, we used the accelerated refraction-corrected (ARC) image reconstruction technique as the representative of the methods that use the position and geometry of the bone layer for aberration correction [34]. This approach is not iterative, and the image grid points are used to describe the near and far surfaces of the bone layer and find the shortest travel-time connecting a pixel to an array element (Fermat's principle). While this allows faster calculation of the travel-times and real-time image reconstruction with a GPU, there are more accurate ray-tracing methods (such as fast marching technique) that could outperform ARC at the expense of a higher processing time [31–33,44].

An ultrafast imaging sequence with a small number of transmit unfocused beams (such as five steered plane waves) might not provide optimal resolution for accurately segmenting the near and far surfaces of the temporal bone layer. To improve the performance of the GB method, a single-element synthetic aperture imaging sequence could be used first to estimate the position and geometry of the bone layer. Then, this information can be used for correcting the phase aberration when imaging with the ultrafast imaging sequence (multi-angle plane waves or diverging waves). Moreover, a transducer operating at an ultrasound frequency higher than 2.5 MHz may help to determine the position and geometry of thin temporal bones (close to 1 mm thickness).

As with the PS method, the performance of the GB method applied to a real temporal bone with complex three-dimensional shape would improve with a two-dimensional matrix array transducer. With such a transducer, the three-dimensional position and geometry of the bone layer could be determined. This would enable accurate three-dimensional ray tracing and, therefore, optimal phase aberration correction.

5. Conclusions

In this paper, we compared two phase aberration correction techniques (near-field phase-screen modeling (PS) and geometry-based reconstruction technique (GB)) when an ultrafast imaging sequence (five plane waves tilted from -15 to 15 degrees in cutaneous tissue) was used for data acquisition. The numerical results showed that the PS technique is strongly affected by speckle noise caused by a heterogeneous brain tissue model and fails to reveal many scatterers in the reconstructed image, while the GB method detects nearly all the scatterers. Compared to the PS approach, the GB method improves the signal-to-clutter ratio by 7.5 dB and reduces the localization error by up to 2 mm in our experimental study. The spatial lateral resolution is only slightly improved by 0.1 mm with the GB method in the experimental study compared with the PS approach. This work indicates that the GB method outperforms the PS method in the case of ultrafast transcranial ultrasound imaging with a single phased-array transducer used for data acquisition.

Author Contributions: Conceptualization, M.M. and G.R.; methodology, M.M. and G.R.; software, M.M. and G.R.; validation, M.M., G.R., N.d.J. and M.D.V.; formal analysis, M.M., G.R., N.d.J. and M.D.V.; investigation, M.M., G.R. and N.d.J.; resources, M.M., G.R., N.d.J. and M.D.V.; data curation, M.M. and G.R.; writing—original draft preparation, M.M. and G.R.; writing—review and editing, G.R., N.d.J. and M.D.V.; visualization, G.R., N.d.J. and M.D.V.; supervision, G.R., N.d.J. and M.D.V.; project administration, N.d.J. and M.D.V.; funding acquisition, N.d.J. and M.D.V. All authors have read and agreed to the published version of the manuscript.

Funding: This work was supported by a joint grant from the Netherlands Organisation for Scientific Research (NWO)/the Netherlands Organisation for Health Research and Development (ZonMw) and the Department of Biotechnology (Government of India) under the program Medical Devices for Affordable Health (MDAH) as Project Imaging Needles (Grant Number 116310008).

Institutional Review Board Statement: Not applicable.

Informed Consent Statement: Not applicable.

Data Availability Statement: The numerical and experimental data used in this study will be provided upon request.

Acknowledgments: This work was supported by a joint grant from the Netherlands Organisation for Scientific Research (NWO)/the Netherlands Organisation for Health Research and Development (ZonMw) and the Department of Biotechnology (Government of India) under the program Medical Devices for Affordable Health (MDAH) as Project Imaging Needles (Grant Number 116310008).

Conflicts of Interest: The authors declare no conflict of interest.

References

1. Hölscher, T.; Schlachetzki, F.; Zimmermann, M.; Jakob, W.; Ittner, K.P.; Haslberger, J.; Bogdahn, U.; Boy, S. Transcranial Ultrasound from Diagnosis to Early Stroke Treatment. *Cerebrovasc. Dis.* **2008**, *26*, 659–663. [CrossRef] [PubMed]
2. Schlachetzki, F.; Herzberg, M.; Hölscher, T.; Ertl, M.; Zimmermann, M.; Ittner, K.P.; Pels, H.; Bogdahn, U.; Boy, S. Transcranial Ultrasound from Diagnosis to Early Stroke Treatment—Part 2: Prehospital Neurosonography in Patients with Acute Stroke—The Regensburg Stroke Mobile Project. *Cerebrovasc. Dis.* **2012**, *33*, 262–271. [CrossRef] [PubMed]
3. Holscher, T. Prehospital use of portable ultrasound for stroke diagnosis and treatment initiation. *Air Rescue* **2012**, *2*, 48–50.
4. Antipova, D.; Eadie, L.; Makin, S.; Shannon, H.; Wilson, P.; Macaden, A. The use of transcranial ultrasound and clinical assessment to diagnose ischaemic stroke due to large vessel occlusion in remote and rural areas. *PLoS ONE* **2020**, *15*, e0239653. [CrossRef]
5. Herzberg, M.; Boy, S.; Hölscher, T.; Ertl, M.; Zimmermann, M.; Ittner, K.-P.; Pemmerl, J.; Pels, H.; Bogdahn, U.; Schlachetzki, F. Prehospital stroke diagnostics based on neurological examination and transcranial ultrasound. *Crit. Ultrasound J.* **2014**, *6*, 3. [CrossRef]
6. White, H.; Venkatesh, B. Applications of transcranial Doppler in the ICU: A review. *Intensiv. Care Med.* **2006**, *32*, 981–994. [CrossRef]
7. Adams, R.J. TCD in sickle cell disease: An important and useful test. *Pediatr. Radiol.* **2005**, *35*, 229–234. [CrossRef]
8. Optimizing Primary Stroke Prevention in Sickle Cell Anemia (STOP 2) Trial Investigators. Investigators. Discontinuing prophylactic transfusions used to prevent stroke in sickle cell disease. *N. Engl. J. Med.* **2005**, *353*, 2769–2778. [CrossRef]
9. Adams, R.J.; McKie, V.C.; Hsu, L.; Files, B.; Vichinsky, E.; Pegelow, C.; Abboud, M.; Gallagher, D.; Kutlar, A.; Nichols, F.T.; et al. Prevention of a First Stroke by Transfusions in Children with Sickle Cell Anemia and Abnormal Results on Transcranial Doppler Ultrasonography. *N. Engl. J. Med.* **1998**, *339*, 5–11. [CrossRef]
10. Adams, R.J.; Nichols, F.T.; Figueroa, R.; McKie, V.; Lott, T. Transcranial Doppler correlation with cerebral angiography in sickle cell disease. *Stroke* **1992**, *23*, 1073–1077. [CrossRef]
11. Newell, D.W.; Grady, S.M.; Eskridge, J.M.; Winn, R.H. Distribution of Angiographic Vasospasm after Subarachnoid Hemorrhage: Implications for Diagnosis by Transcranial Doppler Ultrasonography. *Neurosurgery* **1990**, *27*, 574–577. [CrossRef] [PubMed]
12. Vora, Y.Y.; Suarez-Almazor, M.; Steinke, D.E.; Martin, M.L.; Findlay, J.M. Role of transcranial Doppler monitoring in the diagnosis of cerebral vasospasm after subarachnoid hemorrhage. *Neurosurgery* **1999**, *44*, 1237–1248. [PubMed]
13. Fry, F.J.; Barger, J.E. Acoustical properties of the human skull. *J. Acoust. Soc. Am.* **1978**, *63*, 1576–1590. [CrossRef]
14. Vignon, F.; Aubry, J.F.; Tanter, M.; Margoum, A.; Fink, M. Adaptive focusing for transcranial ultrasound imaging using dual arrays. *J. Acoust. Soc. Am.* **2006**, *120*, 2737–2745. [CrossRef] [PubMed]
15. Pinton, G.; Aubry, J.-F.; Bossy, E.; Muller, M.; Pernot, M.; Tanter, M. Attenuation, scattering, and absorption of ultrasound in the skull bone. *Med. Phys.* **2011**, *39*, 299–307. [CrossRef]
16. Brisson, R.T.; Santos, R.D.S.A.; Stefano, L.H.S.S.; Barreira, C.M.A.; Arruda, J.F.D.L.; Dias, F.A.; Camilo, M.R.; Pontes-Neto, O.M. Association between Tomographic Characteristics of the Temporal Bone and Transtemporal Window Quality on Transcranial Color Doppler Ultrasound in Patients with Stroke or Transient Ischemic Attack. *Ultrasound Med. Biol.* **2020**, *47*, 511–516. [CrossRef]
17. Baykov, S.V.; Babin, L.V.; Molotilov, A.M.; Neiman, S.I.; Riman, V.V.; Svet, V.D.; Selyanin, A.I. Physical and technical aspects of ultrasonic brain imaging through thick skull bones: 2. Experimental studies. *Acoust. Phys.* **2003**, *49*, 389–395. [CrossRef]
18. Baikov, S.; Molotilov, A.; Svet, V. Physical and technological aspects of ultrasonic imaging of brain structures through thick skull bones: 1. Theoretical and model studies. *Acoust. Phys.* **2003**, *49*, 276–284. [CrossRef]
19. Dahl, J.; Soo, M.; Trahey, G. Spatial and temporal aberrator stability for real-time adaptive imaging. *IEEE Trans. Ultrason. Ferroelectr. Freq. Control* **2005**, *52*, 1504–1517. [CrossRef]

20. Vignon, F.; Aubry, J.-F.; Tanter, M.; Margoum, A.; Fink, M.; Lecoeur, J. Dual-arrays brain imaging prototype: Experimental in vitro results. In Proceedings of the IEEE International Ultrasonics Symposium, Tours, France, 18–21 September 2016; Volume 1, pp. 504–507. [CrossRef]
21. Ivancevich, N.; Dahl, J.; Trahey, G.; Smith, S. Phase-aberration correction with a 3-D ultrasound scanner: Feasibility study. *IEEE Trans. Ultrason. Ferroelectr. Freq. Control* **2006**, *53*, 1432–1439. [CrossRef]
22. Ivancevich, N.M.; Pinton, G.F.; Nicoletto, H.A.; Bennett, E.; Laskowitz, D.T.; Smith, S.W. Real-Time 3-D Contrast-Enhanced Transcranial Ultrasound and Aberration Correction. *Ultrasound Med. Biol.* **2008**, *34*, 1387–1395. [CrossRef] [PubMed]
23. Ivancevich, N.M.; Dahl, J.J.; Smith, S.W. Comparison of 3-D multi-lag cross-correlation and speckle brightness aberration correction algorithms on static and moving targets. *IEEE Trans. Ultrason. Ferroelectr. Freq. Control* **2009**, *56*, 2157–2166. [CrossRef] [PubMed]
24. Wang, T.; Jing, Y. Transcranial ultrasound imaging with speed of sound-based phase correction: A numerical study. *Phys. Med. Biol.* **2013**, *58*, 6663–6681. [CrossRef]
25. Lin, X.; Sun, M.; Liu, Y.; Shen, Z.; Shen, Y.; Feng, N. Variable speed of sound compensation in the linear-array photoacoustic tomography using a multi-stencils fast marching method. *Biomed. Signal Process. Control* **2018**, *44*, 67–74. [CrossRef]
26. Shapoori, K.; Sadler, J.; Wydra, A.; Malyarenko, E.V.; Sinclair, A.N.; Maev, R.G. An Ultrasonic-Adaptive Beamforming Method and Its Application for Trans-skull Imaging of Certain Types of Head Injuries; Part I: Transmission Mode. *IEEE Trans. Biomed. Eng.* **2014**, *62*, 1253–1264. [CrossRef] [PubMed]
27. Jiang, C.; Li, Y.; Li, B.; Liu, C.; Xu, F.; Xu, K.; Ta, D. Ray Theory-Based Transcranial Phase Correction for Intracranial Imaging: A Phantom Study. *IEEE Access* **2019**, *7*, 163013–163021. [CrossRef]
28. Jing, Y.; Meral, F.C.; Clement, G.T. Time-reversal transcranial ultrasound beam focusing using a k-space method. *Phys. Med. Biol.* **2012**, *57*, 901–917. [CrossRef]
29. Bouchoux, G.; Bader, K.B.; Korfhagen, J.J.; Raymond, J.L.; Shivashankar, R.; A Abruzzo, T.; Holland, C.K. Experimental validation of a finite-difference model for the prediction of transcranial ultrasound fields based on CT images. *Phys. Med. Biol.* **2012**, *57*, 8005–8022. [CrossRef]
30. Jiang, C.; Li, Y.; Xu, K.; Ta, D. Full-Matrix Phase Shift Migration Method for Transcranial Ultrasonic Imaging. *IEEE Trans. Ultrason. Ferroelectr. Freq. Control* **2020**, *68*, 72–83. [CrossRef]
31. Mozaffarzadeh, M.; Verschuur, E.; Verweij, M.D.; Daeichin, V.; De Jong, N.; Renaud, G. Refraction-Corrected Transcranial Ultrasound Imaging Through the Human Temporal Window Using a Single Probe. *IEEE Trans. Ultrason. Ferroelectr. Freq. Control* **2022**, *69*, 1191–1203. [CrossRef]
32. Renaud, G.; Kruizinga, P.; Cassereau, D.; Laugier, P. In vivo ultrasound imaging of the bone cortex. *Phys. Med. Biol.* **2018**, *63*, 125010. [CrossRef] [PubMed]
33. Renaud, G.; Clouzet, P.; Cassereau, D.; Talmant, M. Measuring anisotropy of elastic wave velocity with ultrasound imaging and an autofocus method: Application to cortical bone. *Phys. Med. Biol.* **2020**, *65*, 235016. [CrossRef] [PubMed]
34. Mozaffarzadeh, M.; Verschuur, E.; Verweij, M.D.; De Jong, N.; Renaud, G. Accelerated 2D Real-Time Refraction-Corrected Transcranial Ultrasound Imaging. *IEEE Trans. Ultrason. Ferroelectr. Freq. Control* **2022**, *69*, 2599–2610. [CrossRef] [PubMed]
35. Hong, D. Medical Image Segmentation Based on Accelerated Dijkstra Algorithm. In *Advances in Intelligent Systems*; Springer: Berlin/Heidelberg, Germany, 2012; Volume 138, pp. 341–348. [CrossRef]
36. Qiu, W.; Bouakaz, A.; Konofagou, E.E.; Zheng, H. Ultrasound for the brain: A review of physical and engineering principles, and clinical applications. *IEEE Trans. Ultrason. Ferroelectr. Freq. Control* **2020**, *68*, 6–20. [CrossRef] [PubMed]
37. Demené, C.; Robin, J.; Dizeux, A.; Heiles, B.; Pernot, M.; Tanter, M.; Perren, F. Transcranial ultrafast ultrasound localization microscopy of brain vasculature in patients. *Nat. Biomed. Eng.* **2021**, *5*, 219–228. [CrossRef]
38. Montaldo, G.; Tanter, M.; Fink, M. Time Reversal of Speckle Noise. *Phys. Rev. Lett.* **2011**, *106*, 054301. [CrossRef] [PubMed]
39. Flax, S.; O'Donnell, M. Phase-aberration correction using signals from point reflectors and diffuse scatterers: Basic principles. *IEEE Trans. Ultrason. Ferroelectr. Freq. Control* **1988**, *35*, 758–767. [CrossRef]
40. Rigby, K.W.; Chalek, C.L.; Haider, B.H.; Lewandowski, R.S.; O'Donnell, M.; Smith, L.S.; Wildes, D.G. Improved in vivo abdominal image quality using real-time estimation and correction of wavefront arrival time errors. In Proceedings of the 2000 IEEE Ultrasonics Symposium. Proceedings. An International Symposium (Cat. No. 00CH37121), San Juan, PR, USA, 22–25 October 2000; Volume 2, pp. 1645–1653.
41. Treeby, B.E.; Cox, B.T. k-Wave: MATLAB toolbox for the simulation and reconstruction of photoacoustic wave fields. *J. Biomed. Opt.* **2010**, *15*, 021314. [CrossRef]
42. Jing, B.; Lindsey, B.D. Effect of Skull Porous Trabecular Structure on Transcranial Ultrasound Imaging in the Presence of Elastic Wave Mode Conversion at Varying Incidence Angle. *Ultrasound Med. Biol.* **2021**, *47*, 2734–2748. [CrossRef]
43. Chandrasekaran, S.; Tripathi, B.B.; Espindola, D.; Pinton, G.F. Modeling Ultrasound Propagation in the Moving Brain: Applications to Shear Shock Waves and Traumatic Brain Injury. *IEEE Trans. Ultrason. Ferroelectr. Freq. Control* **2020**, *68*, 201–212. [CrossRef]
44. Shepherd, J.; Renaud, G.; Clouzet, P.; van Wijk, K. Photoacoustic imaging through a cortical bone replica with anisotropic elasticity. *Appl. Phys. Lett.* **2020**, *116*, 243704. [CrossRef]